The Astrophysical Journal, 1007:113 (10pp), 2026 August 20 https://doi.org/10.3847/1538-4357/ae8aec

Recurrent Multiyear Mg II Broad Absorption Line Variability in SDSS J1333+0012

M. Vivek[1,2], P. Aromal[3,4], R. Srianand[5], K. A. Anjali[1], S. C. Gallagher[3,4], and Rachana[1,6]
[1] Indian Institute of Astrophysics, Koramangala II block, Bangalore 560034, India; vivek.m@iiap.res.in
[2] Astronomisches Rechen-Institut, Zentrum fur Astronomie der Universitat Heidelberg, Monchhofstr. 12-14, D-69120 Heidelberg, Germany
[3] Physics and Astronomy Department, University of Western Ontario, 1151 Richmond Street, London, N6A 3K7, Ontario, Canada
[4] Institute for Earth and Space Exploration, Western University, 1151 Richmond Street, London, ON N6A 3K7, Canada
[5] IUCAA, Postbag 4, Ganeshkind, Pune 411007, India
[6] Joint Astronomy Programme, Department of Physics, Indian Institute of Science, Bangalore 560012, India
Received 2026 April 24; revised 2026 July 13; accepted 2026 July 13; published 2026 August 11

Abstract

We present a long-term spectroscopic study of broad absorption line (BAL) variability in the quasar J1333+0012 (z_{em} = 0.9197) using an extensive multiepoch dataset spanning nearly two decades. The dataset comprises multiepoch observations from multiple observatories, delivering nearly uniform temporal coverage of the Mg II BAL profile, with close to one spectroscopic observation per year spanning the period from 2008 to 2025. We identify recurrent multiyear variability in the BAL absorption strength, characterized by a rest-frame timescale of ∼4 yr. Because the well-sampled baseline covers only a small number of candidate cycles, we present J1333+0012 as a candidate quasiperiodic BAL system. In contrast, contemporaneous optical photometric light curves from CRTS, Pan-STARRS, and Zwicky Transient Facility show no statistically significant correlated variability on comparable timescales. However, ionization-driven variability cannot be ruled out, as the observed optical continuum does not directly trace the unobserved extreme-UV ionizing continuum. The coherence of the variability across distinct velocity components, coupled with the absence of large-scale profile reshaping, is consistent with a geometric origin. We interpret the observed behavior as modulation of the line-of-sight absorption by the rotation of an inhomogeneous shielding-gas structure.

Unified Astronomy Thesaurus concepts: Broad-absorption line quasar (183); Active galactic nuclei (16); Ultraviolet spectroscopy (2284); Active galaxies (17); Quasars (1319)

1. Introduction

Outflows from active galactic nuclei (AGN) are now recognized as a fundamental component of black hole–galaxy coevolution. AGN-driven winds carry mass, momentum, and energy from near the supermassive black hole into the host galaxy. These winds can influence star formation, redistribute interstellar gas, and explain the tight correlation between black hole mass and the properties of their host galaxies (A. C. Fabian 2012; J. Kormendy & L. C. Ho 2013). AGN outflows have been observed over a wide range of spatial scales and wavelengths, ranging from ultrafast X-ray winds at subparsec scales to ionized and molecular outflows at kiloparsec scales, indicating a complex, multiphase feedback cycle (F. Tombesi et al. 2010; C. Cicone et al. 2014).

Broad absorption line (BAL) quasars, identified by blueshifted BALs (exceeding several thousand km s^{-1}) in the optical and ultraviolet spectra of AGN, provide the clearest signatures of powerful AGN outflows along our line of sight (R. J. Weymann et al. 1991). BAL quasars constitute 10%–20% of optically selected quasar samples, but this fraction may be higher due to selection effects, suggesting that BAL outflows are a common feature of quasar activity (P. C. Hewett & C. B. Foltz 2003; P. Hiremath et al. 2025). Based on the ionic species present, BAL quasars are commonly classified into high-ionization BALs (HiBALs), which show only high-ionization lines, and low-ionization BALs (LoBALs), which additionally exhibit absorption from species such as Mg II and Al III. A rare subset, FeLoBALs, further displays absorption from excited and metastable Fe II and Fe III transitions (P. B. Hall et al. 2002).

Time variability of BAL troughs has emerged as a powerful diagnostic of the physical origin, structure, and location of quasar outflows. Multiepoch spectroscopic studies have revealed that BALs frequently vary in equivalent width (EW), depth, and profile shape on rest-frame timescales ranging from months to years (N. Filiz Ak et al. 2013; M. Vivek et al. 2014; K. S. Green et al. 2023; P. Aromal et al. 2025). Two main types of mechanisms are often used to explain this variability: changes in the ionization state of the absorbing gas caused by continuum fluctuations, and geometric effects such as transverse motion of inhomogeneous absorbing structures across the line of sight. Statistical studies have shown that variability often occurs coherently over limited velocity intervals and is more pronounced at higher outflow velocities (N. Filiz Ak et al. 2013; P. Aromal et al. 2023), favoring models involving clumpy or filamentary winds rather than smooth, homogeneous flows. Despite extensive monitoring campaigns, however, most BAL variability appears stochastic, and clear evidence for periodic or quasiperiodic behavior remains elusive.

SDSS J133356.02+001229.1 (hereafter, SDSS J1333+0012; z_{em} = 0.9197) is a LoBAL quasar famously recognized for its variability in the Mg II absorption line. M. Vivek et al. (2012) first reported the transience of its Mg II BAL features, noting the complete disappearance of a low-velocity component (17,000 km s^{-1}) and the emergence of a new, high-velocity component at approximately 28,000 km s^{-1} that evolved significantly over just a few years. In a follow-up study,

M. Vivek et al. (2018) utilized follow-up observations to reveal even more dramatic behavior, where the high-velocity component reemerged and nearly disappeared again within timescales of just a few days to 4.2 yr in the quasar rest frame. These studies attributed the absorption-line variability to changing ionizing flux, potentially caused by variable shielding or individual gas clouds crossing the line of sight.

In this paper, we present a comprehensive analysis of nearly two decades of spectroscopic monitoring of J1333+0012. We combine moderate-resolution spectra obtained from several facilities to construct one of the most detailed long-term Mg II BAL variability datasets for a single quasar. By focusing on the Mg II BAL profile, we examine how the absorption strength and velocity structure evolve over time across different trough components. Our analysis reveals recurrent multiyear BAL EW variations with a characteristic rest-frame timescale of approximately 4 yr. Because the well-sampled baseline covers only a small number of candidate cycles, we treat this behavior as candidate quasiperiodic variability rather than as a confirmed periodic signal.

2. Data and Analysis

Our spectroscopic observations significantly extend the temporal baseline presented in M. Vivek et al. (2012, 2018). The full dataset includes 24 spectra from the Sloan Digital Sky Survey (SDSS), the IUCAA Girawali Observatory (IGO), the Southern African Large Telescope (SALT), and the Dark Energy Spectroscopic Instrument (DESI). We refer to the earlier papers for details of the observations and data-reduction procedures for spectra obtained up to 2016. Following 2016, we resumed monitoring in 2018 and continued obtaining spectra primarily with SALT using the same instrumental configuration as in our previous campaigns. The SALT observations cover the wavelength range 4500−7500 Å with a spectral resolution of approximately 300 km s^{-1}, and we secured at least one epoch per year to ensure consistent temporal sampling of the Mg II BAL region. For all these data, we used data-reduction steps as explained in P. Aromal et al. (2023). In addition to the SALT monitoring, one further epoch each was obtained from SDSS and DESI, providing independent, homogeneously reduced survey-quality spectra. Details of the observing log, including dates, exposure times, and instrumental setups, are provided in Table 1 in the Appendix.

For continuum normalization, we first fit a continuum to the highest signal-to-noise-ratio SDSS spectrum (obtained on MJD 51955) using PyQSOFit (Q. Wu & Y. Shen 2022), which performs a physically motivated spectral decomposition including a power-law continuum, broad emission-line components, and blended pseudo-continuum features such as Fe II emission. For all remaining epochs, we did not refit the continuum independently. Instead, each epoch was aligned to the reference continuum by allowing two controlled transformations: (1) an overall multiplicative scaling factor and (2) a linear spectral tilt while pivoting around a chosen wavelength. The scaling accounts for differences in absolute flux calibration, slit losses, variable observing conditions, and intrinsic continuum variability. The tilt corrects for small differences in spectral slope that can arise from instrumental response variations or residual calibration mismatches. During the alignment process, care was taken to ensure that the continuum regions on both sides of the Mg II BAL trough were consistently matched to those of the reference spectrum. Once all epoch spectra were aligned to the reference spectrum using the transformation above, the reference continuum model was divided by each transformed spectrum to produce the normalized spectra for subsequent analysis. This normalization scheme ensures a uniform continuum definition across all epochs and substantially reduces systematic errors introduced by independent continuum fits. The continuum fits for each epoch and the corresponding continuum-normalized spectra are presented in Figure 4 in the Appendix.

EWs of the Mg II BAL components were measured from the continuum-normalized, rest-frame aligned spectra. We adopted the same definition of absorption components as in M. Vivek et al. (2018), dividing the profile into five regions: R (5028–5100 Å; v ≈−15200 to −19237 km s^{-1}), B1(4925–5000 Å; v ≈−20,800 to −24,980 km s^{-1}) , B2 (4840 Å–4925 Å; v ≈−24,980 to −29,730 km s^{-1}), and B3(4745 Å–4840 Å; v ≈ −29,730 to −35,030 km s^{-1}) components, as well as the combined B-total region.

3. Results

Figure 1 shows the variation of the Mg II BAL EWs as a function of observation date (MJD) for the individual absorption components R (solid/yellow), B1 (dashed/green), B2 (dashed–dotted/blue), B3 (dotted/dark blue), and B-total (dashed–dotted/red) region. All components exhibit significant long-term variability over the full monitoring period, with the B-total component displaying the largest amplitude changes.

The R component displays comparatively modest but structured variability. It begins at EW≈4Å during 2001−2003, declines substantially over 2008−2013, and then restrengthens beginning in 2015. This is followed by another weakening phase around 2020−2021 and a subsequent recovery in the most recent epochs. In contrast, the B absorption components exhibit substantially larger amplitude variations. Both B1 and B2 rise dramatically from near-zero levels in 2001 and undergo alternating strengthening and weakening phases, with pronounced maxima around 2009, 2015, and 2023, and relative minima near 2011 and 2019. The B3 component generally tracks the overall behavior of the blue complex, albeit with somewhat lower amplitude. A caveat is that, for the SALT spectra obtained between 2019 and 2022, the wavelength coverage does not fully encompass the B3 component, and therefore its EW measurements during these epochs should be interpreted with caution. The B-total EW, which integrates the entire blue absorption complex, most clearly illustrates the long-term evolution of the outflow strength. It shows recurrent phases of strengthening and weakening over the 12.9 yr rest-frame monitoring baseline. The strongest maxima occur around 2009, 2015, and 2023, with relative minima near 2011 and 2019. This pattern is suggestive of a characteristic multiyear recurrence timescale.

We then performed a periodicity analysis on the measured EW of the B-total component. Beginning in 2008, the source has been monitored with a nearly annual cadence, providing substantially more uniform temporal coverage compared to the earlier two SDSS epochs. To minimize biases arising from sparse and uneven sampling, we restrict the periodicity analysis to the EW measurements obtained from 2008 onward. A Lomb–Scargle periodogram reveals a prominent peak at a period of 1586 days, with a white-noise false-alarm probability (FAP) of 5.5×10^{-4}. However, this FAP should be interpreted cautiously

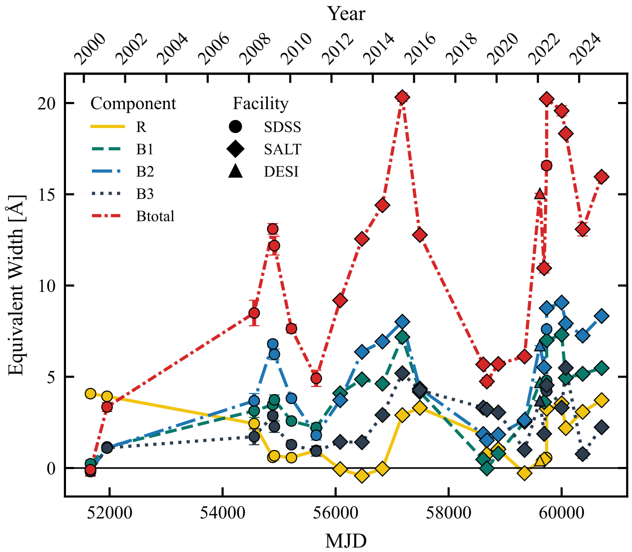

Figure 1. The equivalent widths of the *R* (solid/yellow), B1 (dashed/green), B2 (dashed–dotted/blue), B3 (dotted/dark blue), and B-total (dashed–dotted/red) absorption components are shown as a function of MJD. Marker shapes denote the observing facility: SDSS (circle), IGO (square), SALT (diamond), and DESI (triangle up).

because stochastic red-noise processes, such as damped random walk (DRW) variability, can produce apparently significant periodogram peaks in sparsely sampled light curves.

To investigate the nature of the variability in the B-total EW, we compared three competing models: (1) a purely stochastic DRW model, (2) a purely deterministic sinusoidal model with white noise, and (3) a hybrid model combining a sinusoidal component with a DRW model.

We first fitted the B-total EW time series with two baseline models: a purely stochastic DRW model and a purely deterministic sinusoidal model. The DRW fit was implemented as a Gaussian process (GP), which provides a likelihood-based framework for modeling correlated variability with full propagation of measurement uncertainties. We used the celerite2 implementation of GPs (C. E. Rasmussen & C. K. I. Williams 2006), adopting an exponential covariance kernel (RealTerm) appropriate for a DRW process, $k(\Delta t) = a\, e^{-|\Delta t|/\tau}$, where "a" denotes the DRW process variance and τ is the characteristic damping timescale. Model parameters were optimized by maximizing the GP log-likelihood with physically motivated bounds on τ (i.e [200, 5000] days). In parallel, we fitted a sinusoid-only model assuming independent Gaussian measurement errors, $m(t) = \mu + A \sin(2\pi t/P + \phi)$, where μ is the mean level, A the amplitude, P the period, and ϕ the phase. Finally, we fitted a combined sinusoid+DRW model in which the sinusoidal function represents the mean trend, while the residual variability is modeled as a DRW process. This hybrid framework allows us to assess whether the observed variability is better described by purely stochastic red-noise behavior, coherent periodic modulation, or a combination of both.

Figure 2 shows the rest-frame temporal evolution of the B-total component EW compared with three variability models. The sinusoid-only model captures coherent periodic behavior but does not account for correlated stochastic fluctuations. The shaded regions represent the 1σ uncertainties of the GP components. The inset parameter summaries and corresponding Bayesian information criterion (BIC) values indicate that the hybrid sinusoid+DRW model is statistically preferred over both the purely sinusoidal and DRW-only models (see also Figure 5 in the Appendix, which shows the same analysis for the B2 component alone, which does not suffer from any wavelength coverage issues). The variability is best described as a quasiperiodic modulation superposed on stochastic red-noise variability. The DRW-only model reproduces much of the smooth long-term evolution. For the B-total EW curve, the DRW-only model gives BIC = 178.07, while the sinusoid+DRW model gives BIC = 165.06, corresponding to ΔBIC = 13.01 in favor of the hybrid model. Thus, the sinusoid+DRW model provides a better phenomenological description of the B-total EW variations. However, this improvement should not be interpreted as definitive evidence for a true periodic driver. Additional degrees of freedom can naturally improve the fit to stochastic light curves, and the available temporal baseline spans only a limited number of candidate cycles. We therefore regard the sinusoid+DRW fit as supporting candidate quasiperiodic behavior. In the DRW-only case, a timescale of $\tau \sim 500$ days is physically unlikely if the variability is driven purely by photoionization. Studies of AGN continuum variability using optical light curves show that quasar DRW timescales are typically tens to hundreds of days in the rest frame (C. L. MacLeod et al. 2010). Since τ is often associated with the thermal timescale of the accretion disk, such a large value of $\tau \sim 500$ days would imply an unusually massive supermassive black hole for this source. A more plausible interpretation is that the variability is linked to dynamical processes in the disk wind. Radiatively driven disk-wind simulations by D. Proga (2000) show that the outflow is inherently unstable and develops dense clumps ("density knots") that form through line-driven instabilities and propagate outward. The formation and evolution of these structures occur on year-scale dynamical timescales, which could naturally explain the large effective τ inferred from the DRW modeling. Additionally, a long BAL EW damping timescale can also arise if the absorbing gas responds to continuum variations over a finite recombination or ionization-equilibration timescale (J. H. Krolik & G. A. Kriss 1995; Z. He et al. 2019). In this case, the BAL EW curve would represent a smoothed or low-pass-filtered version of the driving ionizing continuum, and stochastic continuum variability could appear more coherent in the absorption response.

The right panel presents the posterior distributions of the six parameters of the sinusoid+DRW model. The period is constrained to multiyear timescales, while the DRW damping timescale is substantially shorter, demonstrating a separation between coherent modulation and stochastic variability. The marginalized posterior distribution of the period P is broad and skewed, indicating that the period is not tightly constrained by the data. While the posterior favors multiyear periods (of order $\sim$ 1500–2000 rest-frame days), it does not collapse to a narrow peak. This behavior is expected given the limited temporal baseline and the small number of observed cycles. For the same reason, the posterior distribution of the phase parameter, ϕ, is also poorly constrained, reflecting the degeneracy between period and phase when the variability is sampled over a limited time span. The strongest posterior correlation is observed between the DRW hyperparameters, a and τ, reflecting the well-known variance–timescale degeneracy of stochastic processes. The sinusoidal amplitude, A, shows only weak correlations with the DRW parameters, indicating that the periodic component is not strongly absorbed by

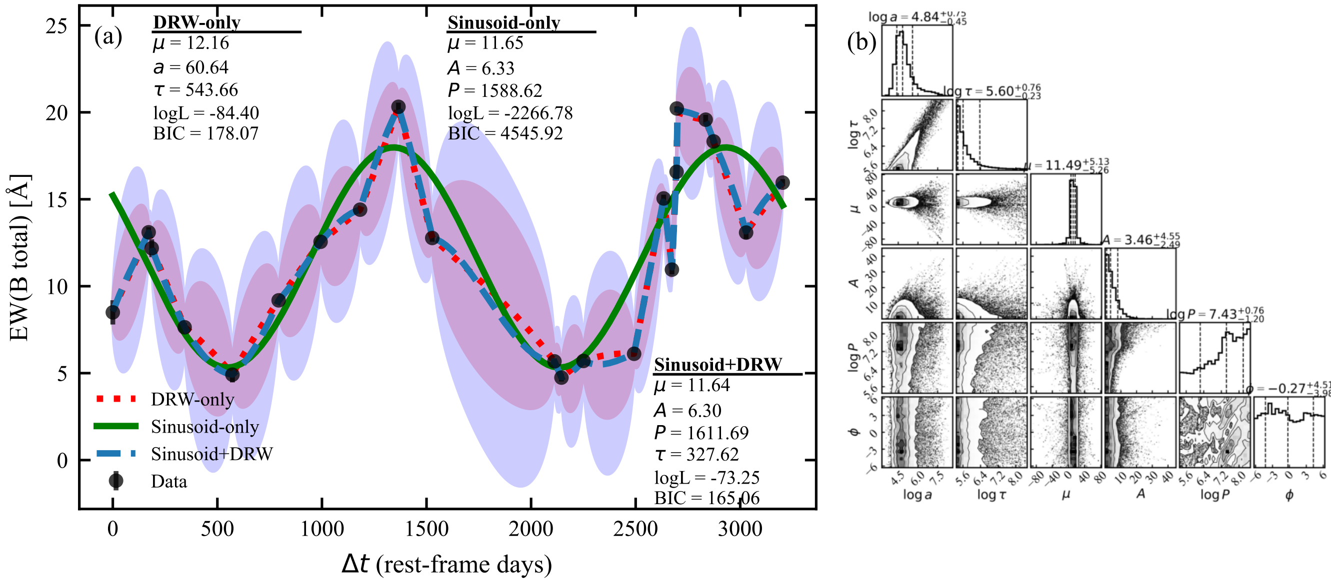

Figure 2. (a) Rest-frame evolution of the B-total equivalent width for J1333+0012 (MJD > 54000), compared with three competing variability models: a damped random walk (DRW; red), a purely sinusoidal model (green), and a combined sinusoid + DRW model (blue). Shaded regions indicate the 1σ predictive uncertainty of the Gaussian process components. The DRW model assumes an exponential covariance kernel with characteristic timescale τ, while the sinusoidal component is parameterized by amplitude A and period P. The inset summaries list the maximum-likelihood parameters and corresponding Bayesian information criterion (BIC) values for each model. (b) Corner plot showing the posterior distributions of the six parameters of the sinusoid + DRW model obtained from Markov Chain Monte Carlo sampling.

adjustments in the stochastic variability. Together, these results indicate that the data are consistent with a multiyear recurrent component, but the period and phase are not tightly constrained by the present baseline. The posterior structure therefore supports a candidate quasiperiodic interpretation rather than a confirmed periodic detection. We compiled the long-term optical light curve of SDSS J1333+0012 using CRTS (V band), Zwicky Transient Facility (ZTF) (g, r, i), and Pan-STARRS (g, r, i, y, z) photometry, spanning nearly two decades in the observed frame, as shown in Figure 3. The source exhibits clear multiyear variability with a peak-to-peak amplitude of ≈0.3–0.6 mag. Spectroscopic epochs used for BAL EW measurements are overplotted as vertical dashed lines. The continuum exhibits smooth secular evolution on multiyear timescales, broadly consistent with accretion-disk-driven variability. No clear correlation between continuum and BAL variability is evident. During the 2020–2025 interval, the BAL absorption shows strong variability, while the contemporaneous ZTF light curve displays only modest flux changes. This already suggests that the BAL evolution is unlikely to be driven solely by continuum ionization changes. Indeed, the ZTF g-band light curve is well described by a DRW process with $\tau = 36$ days (rest frame) and an asymptotic variability amplitude of $SF_{\infty} = 0.035$ mag, values that are entirely typical of optical quasar variability in luminous quasars with $L_{bol} \sim 10^{45}$–10^{47} erg s^{-1} (C. L. MacLeod et al. 2010). The inferred stochastic continuum variability amplitude is therefore only ∼3%. By contrast, the BAL absorption strength exhibits much larger variations and quasiperiodic behavior on multiyear timescales, pointing to the presence of an additional mechanism beyond standard stochastic continuum fluctuations.

Another possible way to test an ionization-driven scenario is to compare the Mg II BAL EW directly with the continuum flux measured from the spectra. Such a test is most straightforward when the absorption is not strongly saturated, since in saturated BAL troughs the EW may be governed

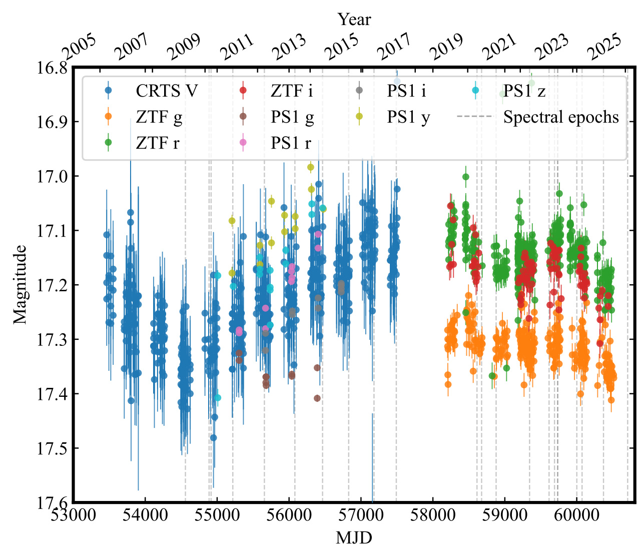

Figure 3. Optical light curve of SDSS J1333+0012 combining CRTS (V band), ZTF (g, r, i), and Pan-STARRS (g, r, i, y, z) photometry. Magnitudes are plotted in the observed frame as a function of MJD. Vertical dashed lines mark the spectroscopic epochs used for BAL equivalent-width measurements.

primarily by covering fraction rather than by changes in ionic column density. Therefore, any EW–continuum comparison should be interpreted with this limitation in mind. In the present case, an additional practical limitation is that a significant fraction of our monitoring data were obtained with SALT, whose moving-pupil design and variable effective aperture prevent reliable absolute spectrophotometric calibration between epochs. Continuum fluxes measured directly from the SALT spectra are therefore affected by aperture-, throughput-, and observing-condition-dependent uncertainties that are unrelated to intrinsic quasar variability. For this reason, we do not consider the spectroscopic continuum fluxes to be a robust tracer of the intrinsic source continuum level for interepoch correlation analysis, and we avoid using them to compute the BAL EW–spectroscopic-continuum correlation.

As an alternative, we used the ZTF light curves as an external photometric continuum proxy for the post-2018 spectroscopic epochs. For the 11 epochs with contemporaneous ZTF coverage, we matched each spectroscopic MJD to the ZTF photometry and computed the median magnitude within a $\pm$50 day window. We then compared these matched ZTF magnitudes with the Mg II BAL EWs. This test does not show a statistically significant correlation ($\rho = -0.02$ with p-value of 0.9) between the optical continuum and BAL strength. However, the number of matched epochs is still small, the scatter in the matched ZTF magnitudes is comparable to the typical photometric uncertainties, and the BAL EW may not linearly trace ionic column density if the absorption is saturated or partially saturated. The available optical data do not show evidence for a simple one-to-one relation between observed optical continuum variability and Mg II BAL EW, but ionization variability driven by the unobserved EUV continuum cannot be ruled out.

4. Discussion and Conclusions

Our long-term spectroscopic monitoring of SDSS J1333+0012 reveals recurrent multiyear variability in the Mg II BAL EWs, with a characteristic rest-frame timescale of approximately 4 yr. The recurrence is visible most clearly in the B-total absorption complex and is also reflected, to varying degrees, in the individual velocity components. However, because the well-sampled baseline covers only a small number of candidate cycles, we do not claim a confirmed periodic signal. Instead, we identify J1333+0012 as a candidate quasiperiodic BAL system whose recurrence must be tested with continued monitoring. The variability pattern is recurrent across multiple cycles, yet it exhibits no clear correlation with the optical continuum light curve. The optical continuum does not directly trace the extreme-UV photons that govern the ionization balance of Mg II. Variability in the unobserved EUV continuum could thus drive changes in the absorber's ionization state even in the absence of strong optical continuum variability. Accordingly, ionization-driven variability cannot be excluded based solely on the available optical monitoring data.

An additional striking feature is the opposite behavior of the red and blue BAL components during the early epochs (2001–2009), where strengthening of one component coincides with weakening of the other. If we take at face value that variability in the unobserved EUV continuum drives the ionization changes, the contrasting behavior of the red and blue components can be interpreted as arising from their location on different sides of the column density–ionization parameter (log U) curve. Between 2001 and 2003, the red component is strong—consistent with higher density and lower ionization parameter—while the blue component is weak, likely corresponding to lower density and higher U, leading to opposite responses to the same continuum variations. From 2003 to 2008, as the continuum flux declines, the red component weakens or disappears while the blue strengthens. During 2009–2012, a substantial continuum brightening likely overionizes the red component, causing it to vanish; at the same time, red component may provide partial shielding that prevents complete overionization of the blue component. Between 2012 and 2015, the red component remains weak initially before reemerging as the continuum declines, accompanied by strengthening of the blue absorption. From 2015 to 2020, both components decrease despite increasing continuum flux, suggesting that simple overionization is no longer important. During 2020–2022, a continuum decline coincides with strengthening of both components, while the 2022–2025 interval shows relatively stable continuum and BAL properties. However, this scenario requires a structured absorber in which different velocity components respond differently to the same ionizing continuum. It may also require variations in the unobserved EUV continuum or in the shielding gas that are not directly traced by the optical light curve. We therefore cannot rule out ionization-driven variability, although a simple one-zone response to the observed optical continuum appears insufficient.

An alternative explanation for the observed recurrent BAL variability is azimuthal structure within a rotating disk wind. If we interpret the candidate rest-frame recurrence timescale of 4.34 yr as an orbital timescale, the implied radial location of the absorber can be estimated from Keplerian motion. Using the single-epoch virial black hole mass derived from the DESI spectra via the Y. Shen et al. (2024) prescriptions, we obtain $M_{\rm BH} \sim 6.4 \times 10^9\, M_\odot$ (from Mg II) and $\sim 9.2 \times 10^8\, M_\odot$ (from Hβ). For a $\sim 10^9\, M_\odot$ black hole, a 4.34 yr orbital period corresponds to a radius of order $\sim$15 light-days, placing the absorber well inside the canonical Mg II broad-line region (BLR), whose reverberation lags are typically 50–100 light-days (Y. Homayouni et al. 2020). This would imply that the absorbing gas lies interior to, or deeply embedded within, the BLR, which is difficult to reconcile with standard BLR stratification and ionization structure. Therefore, unless the black hole mass is substantially larger than inferred, a simple picture of a single corotating cloud at the measured period is unlikely. A more plausible scenario may involve multiple azimuthal density enhancements within a structured disk wind, such that the line of sight intersects successive overdensities during rotation. However, maintaining strict periodicity over multiple cycles would still require long-lived, stable azimuthal structures, posing additional challenges for purely dynamical explanations.

A more plausible explanation is variability driven by changes in a structured shielding gas located interior to the BAL outflow. If this shielding material orbits on a timescale comparable to the observed $\sim$4.3 yr recurrence timescale, azimuthal variations in its column density could periodically modulate the EUV flux reaching the absorber. In this scenario, BAL variability is governed by geometric filtering of the ionizing continuum rather than by global continuum changes, and therefore a correlation with the observed optical flux is not expected. The early anticorrelated behavior of the red and blue components may reflect different velocity structures experiencing different shielding conditions, while the later correlated evolution suggests that both components eventually intercept similar ionizing flux. Thus, orbital modulation of a structured shielding layer provides a natural explanation for the recurrent BAL variability without requiring periodic intrinsic EUV luminosity changes. This interpretation is consistent with the shielding gas framework of M. Vivek et al. (2018), in which modest changes in column density and covering fraction can significantly alter the ionization state of low-ionization species such as Mg II, even without large intrinsic continuum variations.

In the cloud-crossing scenario, variability is attributed to individual absorbing clouds transiting the line of sight. However, this interpretation requires a mechanism that repeatedly launches clouds at specific velocities in a quasiperiodic manner, which appears physically unlikely.

As a speculative possibility, recurrent BAL variability could also arise from dynamical perturbations such as a binary black hole or nuclear star cluster inducing tidal structure in the wind, where the observed period may represent a higher harmonic of the orbital timescale (e.g., from a two-armed spiral), although this remains unconstrained by the present data. Thus, the principal result of this work is the identification of the Mg II BAL in J1333+0012 as a potential candidate for exhibiting quasiperiodic Mg II absorption-line variability. Since periodic variability in BALs has not been observed to date, it is imperative to continue spectroscopic monitoring of J1333+0012 over several additional cycles to confirm and characterize this behavior. The persistence of the predicted strengthening and weakening pattern would support a quasiperiodic interpretation, whereas significant deviations would favor stochastic variability.

Acknowledgments

The authors thank the anonymous referee for the constructive comments that have helped to improve the manuscript. M.V. acknowledges support from DST-SERB in the form of a core research grant (CRG/2022/007884). P.A. and S.C.G. acknowledge support from the Western Research Chair program and Discovery Grant RGPIN-2021-04157 from the Natural Sciences and Engineering Research Council of Canada.

Appendix

The appendix provides supplementary material supporting the main analysis. Table 1 lists the latest SALT spectroscopic observations of SDSS J1333+0012. Figure 4 shows the continuum fits and continuum-normalized spectra for all epochs, and Figure 5 presents the same DRW, sinusoid-only, and sinusoid+DRW comparison as Figure 2, but for the B2 absorption component alone.

Table 1
Log of Latest SALT Spectroscopic Observations of SDSS J1333+0012

Epoch	Year/ Semester	MJD	Exposure Time (s)	Wavelength Coverage (Å)	Resolution (km s^{-1})
SALT	2018B	58613	1200	4750–7790	300
SALT	2019A	58677	1300	4750–7790	300
SALT	2019B	58879	1500	4750–7790	300
SALT	2021A	59344	1500	4750–7790	300
SALT	2021B	59691	1200	4750–7790	300
SALT	2022A	59736	2100	4470–7510	300
SALT	2022B	60001	1400	4470–7510	300
SALT	2023A	60074	1600	4750–7790	300
SALT	2023B	60372	1500	4470–7510	300
SALT	2024B	60708	1400	4470–7510	300

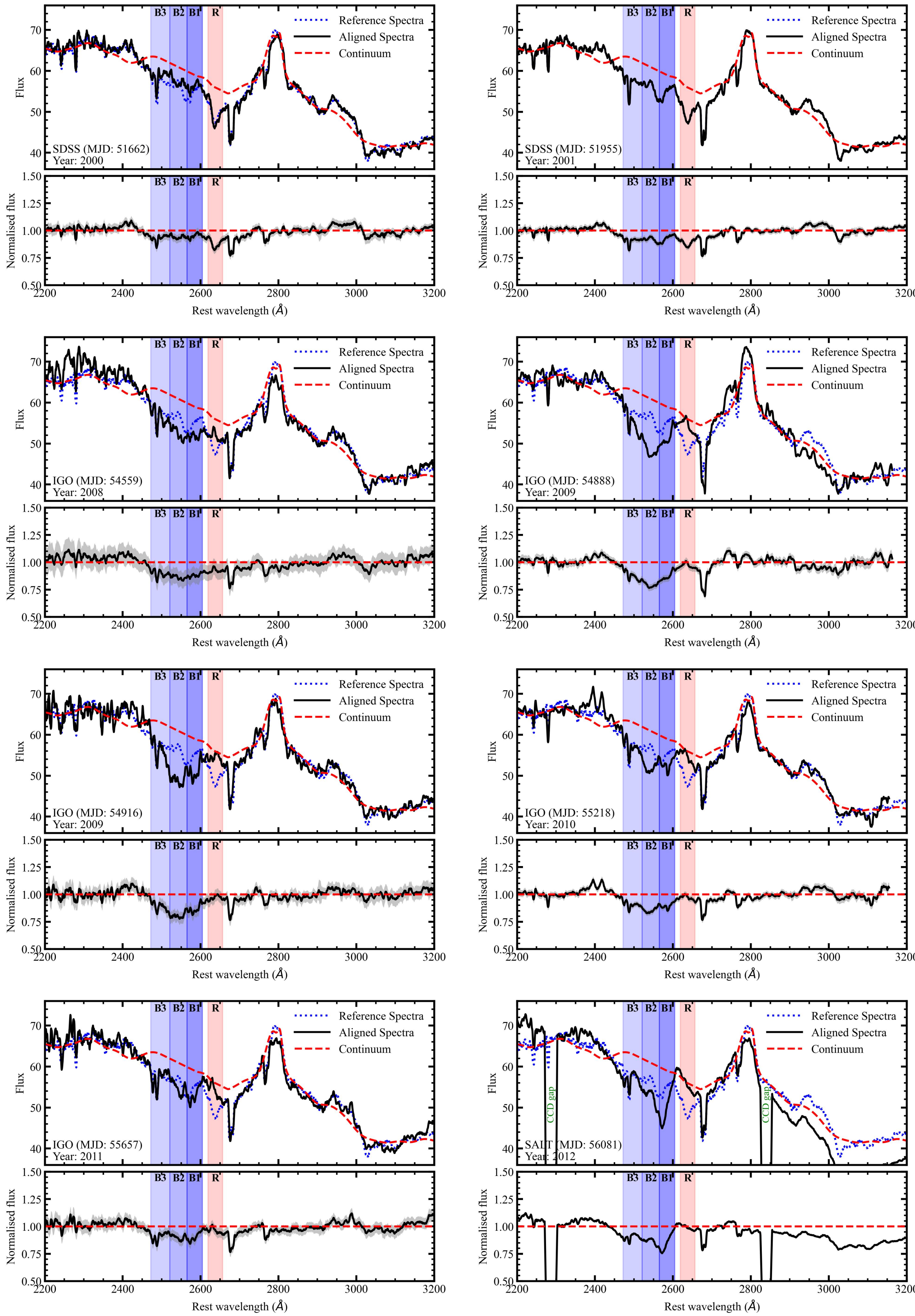

Figure 4. Rest-frame spectra of J1333+0012 shown chronologically. In each panel, the observed spectrum is aligned to the reference SDSS spectrum at MJD 51955, with the fitted continuum overlaid. The lower panels show the continuum-normalized spectra with 1σ uncertainties. Shaded regions mark the Mg II BAL components $B3$, $B2$, $B1$, and R. Narrow absorption redward of the R component is associated with an intervening absorber at $z_{\rm abs} \sim 0.898$.

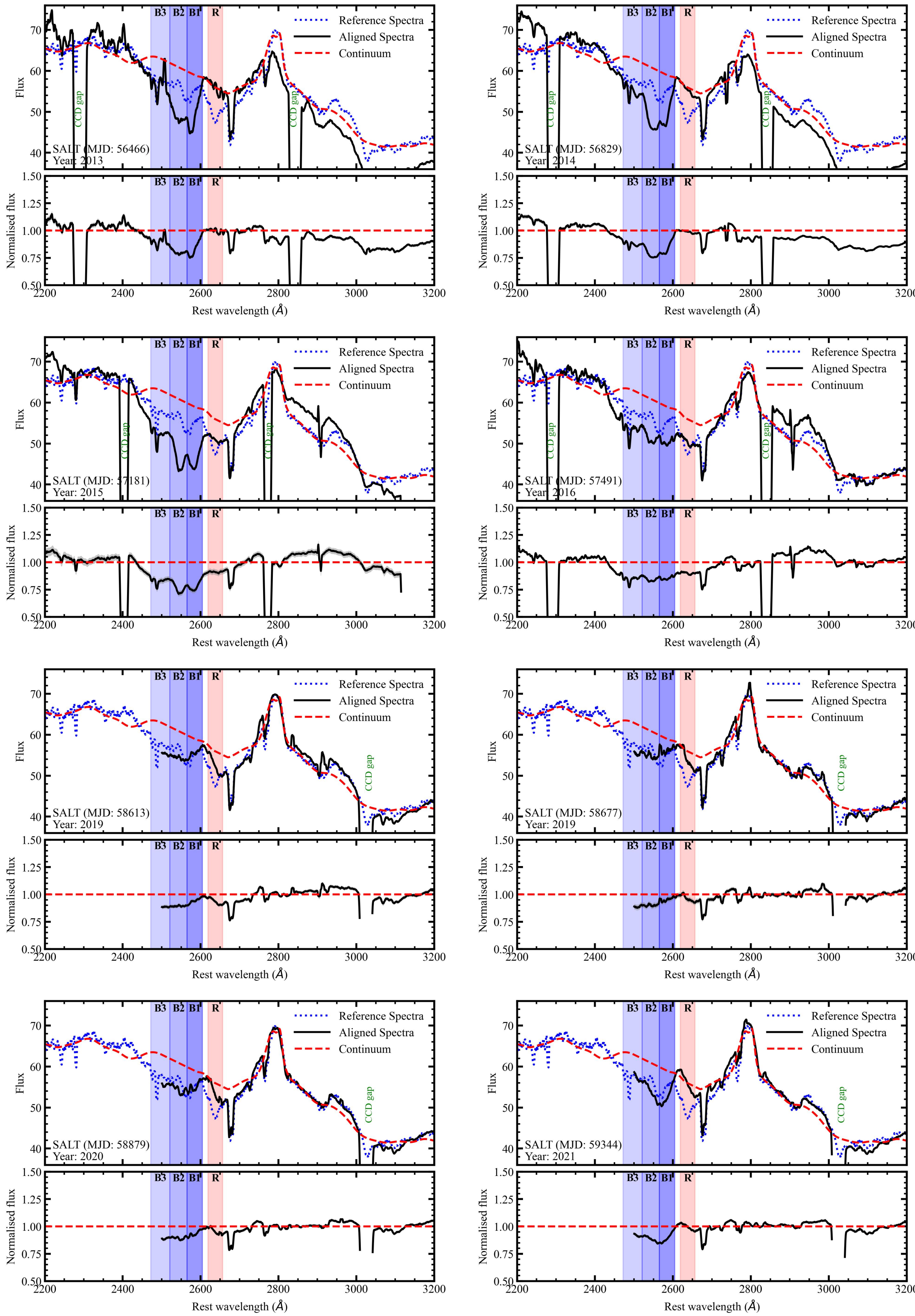

Figure 4. (Continued.)

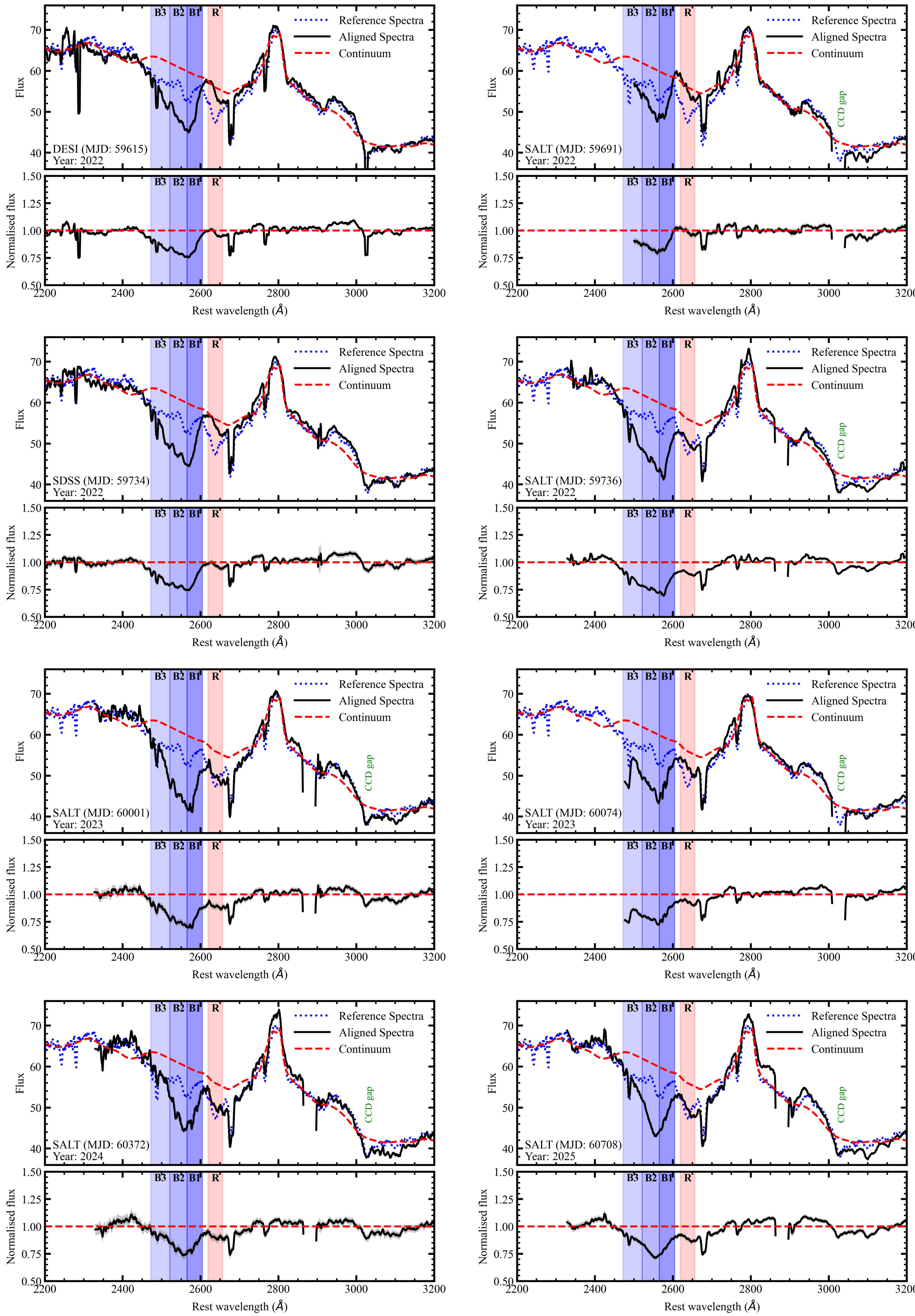

Figure 4. (Continued.)

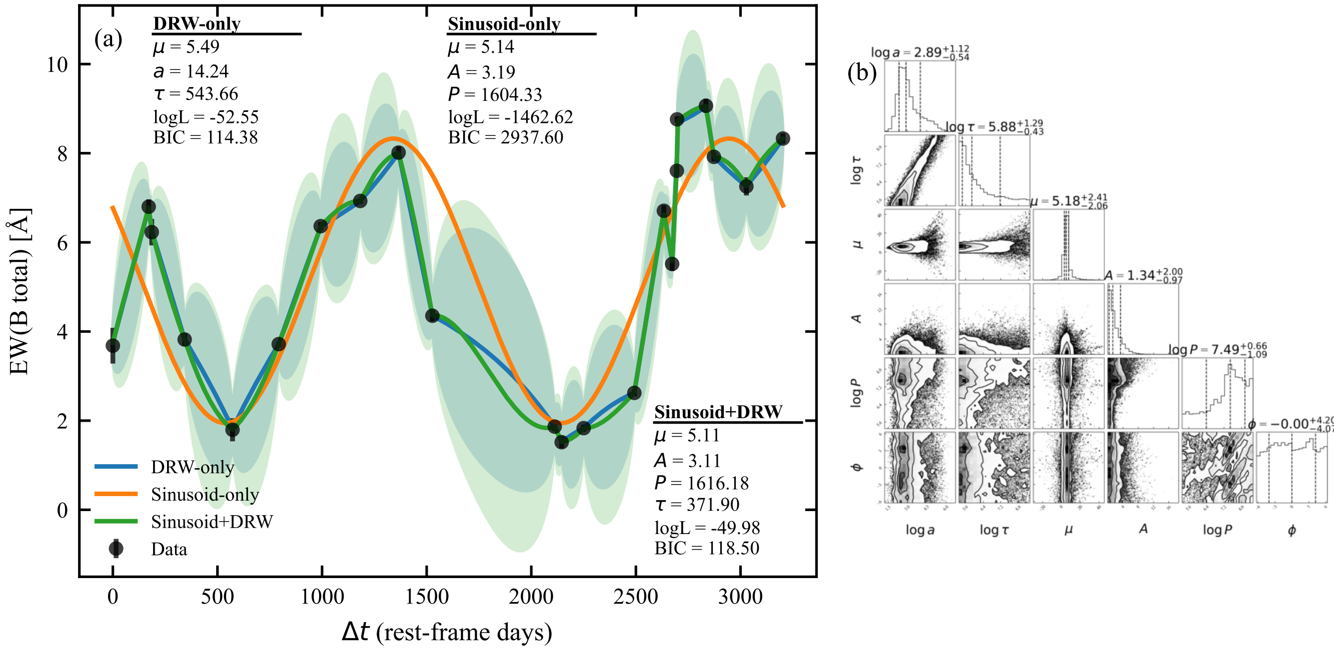

Figure 5. Same as Figure 2, but for the $B2$ component alone.

ORCID iDs

M. Vivek https://orcid.org/0000-0001-5937-331X
P. Aromal https://orcid.org/0009-0001-2178-4022
R. Srianand https://orcid.org/0000-0002-9062-1921
K. A. Anjali https://orcid.org/0009-0008-6712-8734
S. C. Gallagher https://orcid.org/0000-0001-6217-8101
Rachana https://orcid.org/0000-0003-4592-447X

References

Aromal, P., Srianand, R., Gallagher, S. C., Vivek, M., & Petitjean, P. 2025, ApJ, 990, 146
Aromal, P., Srianand, R., & Petitjean, P. 2023, MNRAS, 522, 6374
Cicone, C., Maiolino, R., Sturm, E., et al. 2014, A&A, 562, A21
Fabian, A. C. 2012, ARA&A, 50, 455
Filiz Ak, N., Brandt, W. N., Hall, P. B., et al. 2013, ApJ, 777, 168
Green, K. S., Gallagher, S. C., Leighly, K. M., et al. 2023, ApJ, 953, 186
Hall, P. B., Anderson, S. F., Strauss, M. A., et al. 2002, ApJS, 141, 267
He, Z., Wang, T., Liu, G., et al. 2019, NatAs, 3, 265
Hewett, P. C., & Foltz, C. B. 2003, AJ, 125, 1784
Hiremath, P., Rankine, A. L., Aird, J., et al. 2025, MNRAS, 542, 2105
Homayouni, Y., Trump, J. R., Grier, C. J., et al. 2020, ApJ, 901, 55
Kormendy, J., & Ho, L. C. 2013, ARA&A, 51, 511
Krolik, J. H., & Kriss, G. A. 1995, ApJ, 447, 512
MacLeod, C. L., Ivezić, Ž., Kochanek, C. S., et al. 2010, ApJ, 721, 1014
Proga, D. 2000, ApJ, 538, 684
Rasmussen, C. E., & Williams, C. K. I. 2006, Gaussian Processes for Machine Learning (MIT Press)
Shen, Y., Grier, C. J., Horne, K., et al. 2024, ApJS, 272, 26
Tombesi, F., Cappi, M., Reeves, J. N., et al. 2010, A&A, 521, A57
Vivek, M., Srianand, R., & Dawson, K. S. 2018, MNRAS, 481, 5570
Vivek, M., Srianand, R., Mahabal, A., & Kuriakose, V. C. 2012, MNRAS, 421, L107
Vivek, M., Srianand, R., Petitjean, P., et al. 2014, MNRAS, 440, 799
Weymann, R. J., Morris, S. L., Foltz, C. B., & Hewett, P. C. 1991, ApJ, 373, 23
Wu, Q., & Shen, Y. 2022, ApJS, 263, 42